







Structural insights into TSC complex assembly and GAP activity on Rheb

Huirong Yang^{1,2,3,4,8}✉, Zishuo Yu^{1,8}, Xizi Chen^{1,8}, Jiabei Li¹, Ningning Li⁵ , Jiaxuan Cheng⁵ , Ning Gao⁵ , Hai-Xin Yuan⁶ , Dan Ye⁶, Kun-Liang Guan⁷  & Yanhui Xu^{1,2,3,4}✉ 

Tuberous sclerosis complex (TSC) integrates upstream stimuli and regulates cell growth by controlling the activity of mTORC1. TSC complex functions as a GTPase-activating protein (GAP) towards small GTPase Rheb and inhibits Rheb-mediated activation of mTORC1. Mutations in *TSC* genes cause tuberous sclerosis. In this study, the near-atomic resolution structure of human TSC complex reveals an arch-shaped architecture, with a 2:2:1 stoichiometry of TSC1, TSC2, and TBC1D7. This asymmetric complex consists of two interweaved TSC1 coiled-coil and one TBC1D7 that spans over the tail-to-tail TSC2 dimer. The two TSC2 GAP domains are symmetrically cradled within the core module formed by TSC2 dimerization domain and central coiled-coil of TSC1. Structural and biochemical analyses reveal TSC2 GAP-Rheb complementary interactions and suggest a catalytic mechanism, by which an asparagine thumb (N1643) stabilizes γ -phosphate of GTP and accelerate GTP hydrolysis of Rheb. Our study reveals mechanisms of TSC complex assembly and GAP activity.

¹Fudan University Shanghai Cancer Center, Institutes of Biomedical Sciences, State Key Laboratory of Genetic Engineering and Shanghai Key Laboratory of Medical Epigenetics, Shanghai Medical College of Fudan University, Shanghai 200032, China. ²The International Co-laboratory of Medical Epigenetics and Metabolism, Ministry of Science and Technology, China, Department of Systems Biology for Medicine, School of Basic Medical Sciences, Shanghai Medical College of Fudan University, Shanghai 200032, China. ³Human Phenome Institute, Collaborative Innovation Center of Genetics and Development, School of Life Sciences, Fudan University, Shanghai 200433, China. ⁴State Key Laboratory of Reproductive Regulation and Breeding of Grassland Livestock School of Life Sciences, Inner Mongolia University, Hohhot 010070, China. ⁵State Key Laboratory of Membrane Biology, Peking-Tsinghua Joint Center for Life Sciences, School of Life Sciences, Peking University, 100871 Beijing, China. ⁶The Molecular and Cell Biology Research Lab, The Shanghai Key Laboratory of Medical Epigenetics, Institutes of Biomedical Sciences, Fudan University, Shanghai 200032, China. ⁷Department of Pharmacology and Moores Cancer Center, University of California San Diego, La Jolla, CA, USA. ⁸These authors contributed equally: Huirong Yang, Zishuo Yu, Xizi Chen. ✉email: yanghr@fudan.edu.cn; xuyh@fudan.edu.cn

The mechanistic target of rapamycin complex 1 (mTORC1) is a master regulator of cell growth by phosphorylating a variety of substrates, as exemplified by ribosomal S6 kinase 1 (S6K1) and eukaryote initiation factor 4E binding protein^{1,2}. As a well-known tumor suppressor, the tuberous sclerosis complex (TSC) integrates cues of growth factors, energy status, and various stress to maintain Ras homolog enriched in brain (Rheb) in GDP-bound state, and therefore keeps mTORC1 in check to limit undesirable cell growth^{2–5}. The TSC complex acts as a GTPase-activating protein (GAP) toward a small G-protein Rheb required for mTORC1 activation⁶. In GTP-bound state, Rheb directly binds to and activates mTORC1^{7–11}.

The TSC complex consists of tuberous sclerosis complex 1 (TSC1), tuberous sclerosis complex 2 (TSC2), and an auxiliary subunit Tre2-Bub2-Cdc16-1 domain family member 7 (TBC1D7)^{4,5}. Mutations of TSC1 or TSC2 genes cause tuberous sclerosis, an autosomal dominant genetic disease characterized by the development of histologically diverse hamartomas or benign tumors, including skin, brain, and kidneys^{5,12}. TSC patients are frequently associated with severe neurological manifestations, including epilepsy, intellectual disability, and autism^{5,13}. Although the functions of TSC complex have been extensively studied for decades, there are only a few structures of isolated domains, including TSC1 peptide bound to TBC1D7^{3,14}, N-terminal domains of yeast TSC1¹⁵ and TSC2 (*Chaetomium thermophilum*)¹⁶, and recently reported TSC2 (*Chaetomium thermophilum*) GAP domain structure¹⁷. The lack of TSC complex structure has hampered understanding the mechanisms of complex assembly, GAP activity, and disease correlation.

Here we present the first cryo-EM structure of human TSC complex and elaborate on its characteristic assembly and GAP function. We propose a model of Rheb-bound TSC complex based on structural superimposition with GTP-bound Rheb¹⁸ and Rap1–Rap1GAP¹⁹ structures. Our structure also provides a framework for understanding the regulation of TSC complex function in mTORC1 pathway and its pathological significance.

Results

Structure determination. To obtain TSC complex structure, we overexpressed human TSC1, TSC2, and TBC1D7 in Expi293F cells and purified the complex to homogeneity (Supplementary Fig. 1a). The purified TSC complex showed relatively weak in vitro GAP activity against Rheb, consistent with the known weak in vitro activity^{8,19} (Supplementary Fig. 1b). The structure was determined by cryo-EM single particle reconstruction, and the cryo-EM map was refined to an overall resolution of 4.4 Å (Fig. 1b). The core and two wings were locally refined to 3.6, 3.9, and 4.1 Å resolution, respectively (Supplementary Figs. 2 and 3). The majority of structural model was unambiguously built ab initio aided by the structure of TSC1 fragment bound to TBC1D7¹⁴ and secondary structure analyses (Table 1 and Supplementary Movies 1–4). Residues of TSC1 (876–971), TSC2 (127–936, 1015–1082, 1182–1245, 1494–1732), and TBC1D7 (21–287) were traced and modeled with a TSC2a region (residues 127–315) and TSC1 (residues 746–875) being replaced by poly alanine due to the relatively weak cryo-EM density (Fig. 1a and Supplementary Fig. 4).

Overall structure of human TSC complex. The TSC complex consists of a central core and two wings (termed wing-a and wing-b) and the overall structure exhibits an elongated arch-shaped fold with approximate dimensions of $\sim 390 \times 133 \times 88 \text{ \AA}^3$ (Fig. 1b). TSC1, TSC2, and TBC1D7 assemble the TSC complex with a 2:2:1 stoichiometry, generating an asymmetric modular organization. The overall architecture of TSC1–TSC2 and TSC1–TBC1D7 interactions together allows one TBC1D7 to be

assembled into TSC complex and this subunit stoichiometry is consistent with previous structural and biochemical analyses^{3,14}. Although isolated domains adopt similar folds, the two TSC1 (termed TSC1a/1b) and two TSC2 (TSC2a/2b) reveal distinct conformations, respectively (Supplementary Fig. 5). The two TSC2 molecules form a pseudo-symmetric dimer through tail-to-tail interactions. The coiled-coil domains (CCs, residues 746–971) of TSC1a and TSC1b interwind in parallel and form an extended two-helix bundle with the dimer interface being as much as 2386 Å² (Fig. 1c and Supplementary Fig. 6a–d). The TSC1 dimer makes multiple contacts with TSC2 dimer and stabilizes the overall conformation of the complex. This parallel dimerization of TSC1 leads to an asymmetric formation of TSC1–TSC2 tetramer and recruitment of a single TBC1D7 molecule, generating a unique and characteristic modular organization (Fig. 1b and Supplementary Fig. 5f, g).

Each TSC2 consists of a HEAT repeat domain (HEAT), a dimerization domain (DD), followed by a C-terminal GAP catalytic domain (GAP) (Fig. 1a, b, d). The N-terminal 12 HEAT repeats (wing HEAT, wHEAT) flank out of the central core and are stabilized by TSC1. The following six HEAT repeats (core HEAT, cHEAT) associate with and are stabilized by the central GAP and DD domains. The cHEAT–DD–GAP of the two TSC2 molecules adopt pseudo-symmetric fold, whereas the two wHEAT domains adopt distinct conformations due to differently associated TSC1 (Supplementary Fig. 5). TSC2a and TSC2b bind the N-terminal (N-CC) and C-terminal (C-CC) halves of the TSC1 CC dimer, respectively (Fig. 1b).

The TBC1D7 associates with and stabilizes the C-terminal helices (residues 937–971) of TSC1a/1b but has no direct contact with TSC2. The TBC1D7–TSC1a/1b module adopts a similar fold to the human TSC1–TBC1D7 crystal structure¹⁴ (Supplementary Fig. 6e), and is positioned far away from the central core, consistent with its auxiliary role in TSC complex assembly and function⁴. The observation agrees with the immunoprecipitation results showing that TBC1D7 binds TSC1 but not TSC2 (Supplementary Fig. 6f).

TSC1 structure and its interaction with TSC2. The two CC domains of TSC1a and TSC1b are paired in parallel and form a two-turn left-handed supercoil (Fig. 1c). The pairwise CC involves extensive intermolecular contacts. The TSC1 homodimer interface is enriched in nonpolar residues, which make extensive hydrophobic contacts to support a stable TSC1 dimerization and its scaffolding function (Supplementary Fig. 6a–d).

The TSC1 CC dimer adopts an arch-shaped architecture and packs against the ridge of TSC2 dimer (Figs. 1b and 2a). The CC dimer makes four major contacts with TSC2. (1) The central region of TSC1a (residues 800–890) sits on a “saddle” formed by TSC2 DD dimer (Fig. 2b, c). (2) The TSC1a–N-CC (residues 746–795) packs against the ridge of repeats HEAT7–HEAT12 of TSC2a (Fig. 2d). (3) The C-CC (residues 890–936) dimer of TSC1 packs against the ridge of the repeats HEAT8–HEAT12 of TSC2b (Fig. 2e). (4) The TSC1a–C-CC (residues 937–971) packs against the ridge of repeats HEAT3–HEAT7 of TSC2b (Fig. 2f), confirmed the known interaction between the N-terminus of TSC2 (residues 1–418) and TSC1^{16,20,21}. Consistent with the asymmetric complex formation, TSC1a plays a major role in binding TSC2 dimer. In support of above structural observation, our immunoprecipitation assay shows that full-length TSC1 binds N-HEAT and weakly associates with DD–GAP but exhibits undetectable interaction with DD or GAP domain of TSC2 (Supplementary Fig. 6i).

Another asymmetric feature of the TSC complex exists around the end of wing-a module. The cryo-EM map reveals repetitive

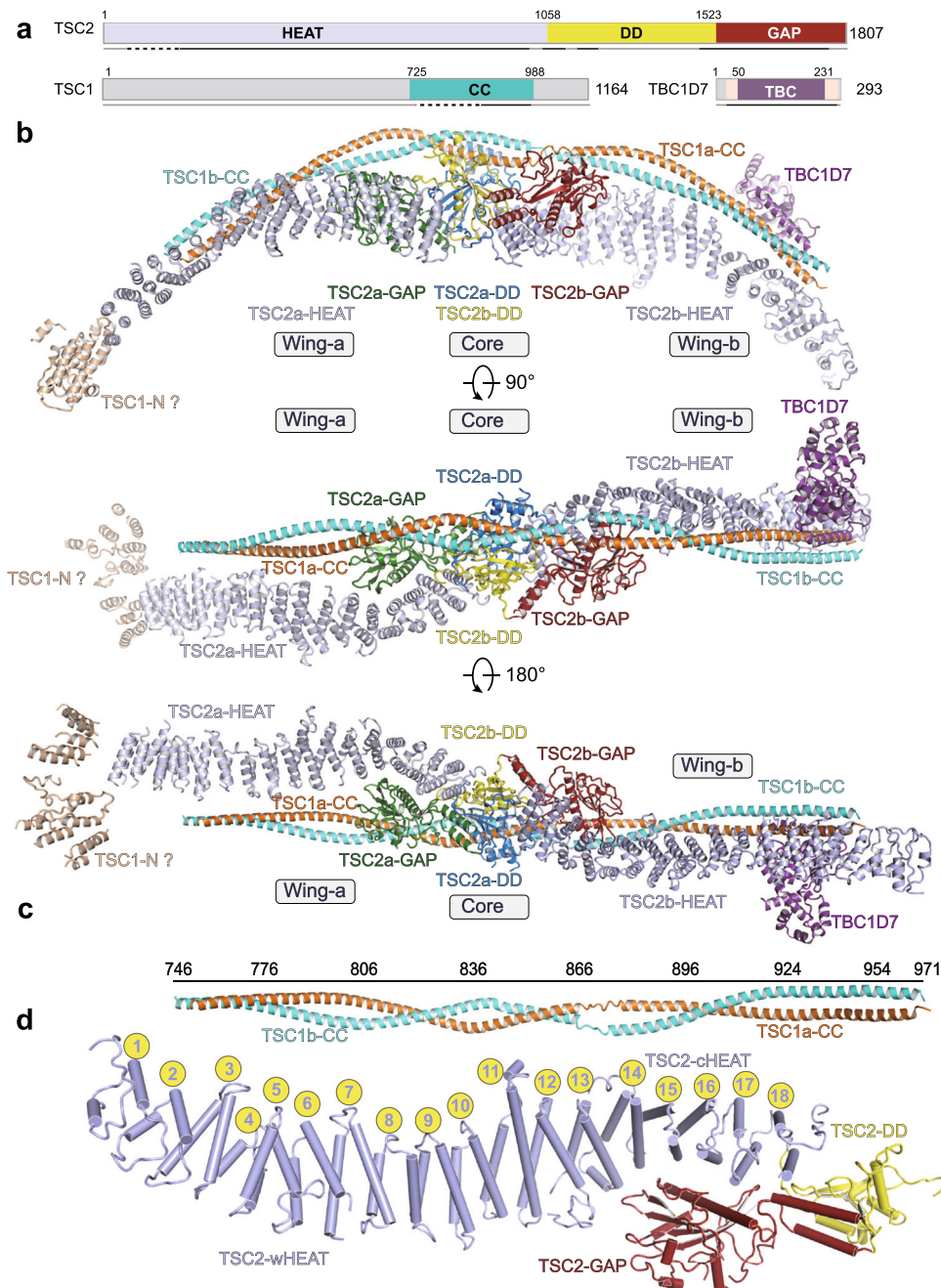


Fig. 1 Overall structure of human TSC complex. **a** Color-coded domain structure of the three subunits with invisible regions colored in gray. Residues at domain boundaries are indicated with numbers. The same color scheme is used throughout all structure figures unless indicated elsewhere. HEAT: HEAT repeat domain, GAP: GTPase-activating domain, CC: coiled coil, DD: dimerization domain, TBC Tre2-Bub2-Cdc16 domain. Residues at domain boundaries are indicated. Unmodeled regions are indicated with gray lines under each protein. Solid black and dashed black lines below indicate regions that were modeled with residues and poly alanine, respectively. **b** Ribbon representation of TSC complex structure in three different views. The modules and subunits are labeled and indicated. **c** TSC1 coiled-coil dimer structure with residue positions indicated. **d** Cartoon model of one of TSC2 monomer, the HEAT repeats are indicated with numbered balls.

helical region covering the N-terminal HEAT repeats of TSC2a but not TSC2b. This region is likely derived from the predicted N-terminal HEAT repeats domain of TSC1 (Fig. 1b and Supplementary Fig. 4b)¹⁵. Other TSC1 regions were invisible in our cryo-EM map due to flexibility. In our immunoprecipitation assay, the full-length and CC of TSC1 shows comparable binding to TSC2 (Supplementary Fig. 6g), consistent with the maintenance of TSC1–TSC2 upon deletion of TSC1 several N-terminal fragments²².

Domain organization and dimerization of TSC2. The TSC2 monomer adopts a seahorse-shaped conformation, in which the wHEAT (HEAT1–HEAT12) and cHEAT (HEAT13–HEAT18) together adopt a right-handed super helical fold (Fig. 1d). In the two TSC2 molecules, the isolated cHEAT and wHEAT domains adopt almost identical conformations, respectively. However, the whole HEAT domain of TSC2b tends to be more extended than that of TSC2a (Supplementary Fig. 5e–g). The two HEAT domains bind the TSC1 dimer in a distinct manner, suggesting

Table 1 Statistics of cryo-EM data collection, refinement, and validation statistics.

	TSC
Data collection and processing	
Magnification	×105,000
Voltage (kV)	300
Electron exposure (e ⁻ /Å ²)	50
Defocus range (μm)	1.0–3.5
Pixel size (Å)	1.356
Symmetry imposed	C1
Initial particle images (No.)	1,528,982
Final particle images (No.)	131,022
Map resolution (Å)	
Consensus reconstruction	4.4
Focus wing-a reconstruction	4.1
Focus core reconstruction	3.6
Focus wing-b reconstruction	3.9
FSC threshold	0.143
Map resolution range (Å)	
Consensus reconstruction	4.0–20.0
Focus wing-a reconstruction	4.0–20.0
Focus core reconstruction	3.0–10.0
Focus wing-b reconstruction	3.0–10.0
Refinement	
Initial model used (PDB code)	5EJC
Model resolution (Å)	4.5
FSC threshold	0.5
Model resolution range (Å)	4.0–4.5
Map sharpening B factor (Å ²)	–129.92
Model composition	
Non-hydrogen atoms	23,934
Protein residues	3089
Ligands	0
B factors (Å ²)	
Protein	141.96
Ligand	–
RMS deviations	
Bond lengths (Å)	0.004
Bond angles (°)	0.673
Validation	
MolProbity score	2.42
Clashscore	24.52
Poor rotamers (%)	0.12
Ramachandran plot	
Favored (%)	90.30
Allowed (%)	9.70
Disallowed (%)	0.00

that different features of N- and C-terminal portions of TSC1 CC dimer lead to distinct conformation of the two TSC2 molecules (Supplementary Fig. 5f).

The cHEAT–DD–GAP parts of two TSC2 molecules form an almost symmetrical core of the complex and the dimerization are mediated by two stably associated DD domains (Fig. 2a–c and Supplementary Fig. 5c–e). Each DD domain consists of a four-stranded antiparallel β-sheet (Dβ1–Dβ4) and five flanking α-helices (Da1–Da5) (Fig. 2c). The two β-sheets together form a saddle-shaped eight-stranded β-sheet. The Da5 helix (residues 1472–1483) packs against the concave surface of the saddle and binds the other TSC2 molecule on HEAT18 and the following loop (residues 1024–1038) (Fig. 2a and Supplementary Fig. 7). The loop preceding helix Da4 inserts into a hydrophobic pocket of the other TSC2 molecule located in a three-way junction formed by the cHEAT, DD, and GAP domains (Fig. 2a). The TSC2 dimerization is further supported by DD helices of the two TSC2 molecules, which sandwich the TSC1a CC domain. Around

this region, the TSC2 dimer interface (~2805 Å²) is larger than TSC1–TSC2 interface (~1761 Å²), suggesting that TSC2 may form a homodimer independent of TSC1 and the TSC2 dimer is required for generating a stable TSC1–TSC2 tetramer²³.

The TSC2 GAP structure and its positioning in TSC complex.

The two GAP catalytic domains are symmetrically cradled within the central core module and each GAP adopts a characteristic mixed α/β fold (Figs. 1b and 3a). A central seven-stranded β-sheet is stabilized by a long α helix (Ga5) from the concave side. The helix Ga3 (catalytic helix) and two loops (L1 and L2) pack against the convex surface of the β-sheet. Three intermolecular contacts involve positioning of each GAP domain (Fig. 3a and Supplementary Fig. 8). (1) Two parallel α helices (GaN and GaC) form a GAP extension, which protrudes out of the catalytic core and binds the edge of the β-sheet of the DD domain and repeats HEAT17–HEAT18 (Supplementary Fig. 8b). (2) The helix Ga5, strand Gβ7, and its preceding loop, together pack against the concave surface of repeats HEAT13–HEAT16 (Supplementary Fig. 8c). (3) The helix Ga1 (TSC2b) or Ga2 (TSC2a) and loop L1 bind TSC1 CC and the binding pattern is slightly different in two GAP domains. The GAP of TSC2a binds single CC (residues 800–830) of TSC1b whereas the GAP of TSC2b binds two CC strands (residues 860–895) of TSC1a/1b (Supplementary Fig. 8d). The lack of TSC1 largely decreased the GAP activity, indicating that TSC1 is required for assembly of fully active GAP domains in TSC complex (Supplementary Fig. 6h). Consistent with above cellular experiments, TSC complex possessed relatively weak GAP activity in the in vitro assay while the isolated TSC2 GAP domain showed undetectable activity (Supplementary Fig. 6j). The two GAP catalytic core adopt almost identical conformations and their catalytic pockets both open outwards, suggesting a similar manner of substrate recognition and catalysis (Fig. 2a and Supplementary Fig. 5d, e).

Catalytic mechanism of TSC2 GAP. The TSC2 GAP domain is highly conserved from yeast to human and shares considerable sequence homology to Rap1GAP (Supplementary Fig. 9a), suggesting that TSC2-stimulated GTP hydrolysis of Rheb follows the same mechanism as in Rap–Rap1GAP system^{8,19,21}. To investigate the mechanism of TSC2-stimulated GTP hydrolysis of Rheb, we superimposed our TSC2 GAP structure and Rheb–GTP (PDB: 1XTS)¹⁸ with Rap1–Rap1GAP structure (PDB: 3BRW)¹⁹ and the classical small G-protein Ras–RasGAP (PDB: 1WQ1)²⁴ (Fig. 3b–d). Structural comparison confirms the predicted structural similarity between the GAP domains of TSC2 and Rap1GAP and reveals distinct fold of the associated domains, which may provide substrate specificity (Fig. 3b, c).

Previous structural and biochemical studies of small GTPases and their GAPs have proposed a generally conserved activation mechanism^{25,26}. All the GAP domains provide positively charged residues, neutralize negative charges generated during phosphoryl transfer reactions, and thus accelerate GTP hydrolysis^{25,26}. Ras–RasGAP represents the prototypic small GTPase–GAP system, in which a *trans*-arginine finger (R789 in RasGAP) and a *cis*-glutamine (Q61 in Ras) are critical for catalysis through stabilizing the γ-phosphate in the transition state^{24,27} (Fig. 3e, f). The arginine finger is shared by GAPs of some other Ras superfamily members²⁶. As a representative exception, Rap1–Rap1GAP lacks the arginine finger, but instead, has an asparagine thumb (N290 in Rap1GAP), which stabilizes γ-phosphate and is essential for GAP activity^{19,28} (Fig. 3g, h).

To analyze the structure of TSC2 GAP, we generated a model of Rheb-bound TSC complex through superimposition of TSC2 GAP and GTP-bound Rheb¹⁸ to Rap1–Rap1GAP¹⁹ complex

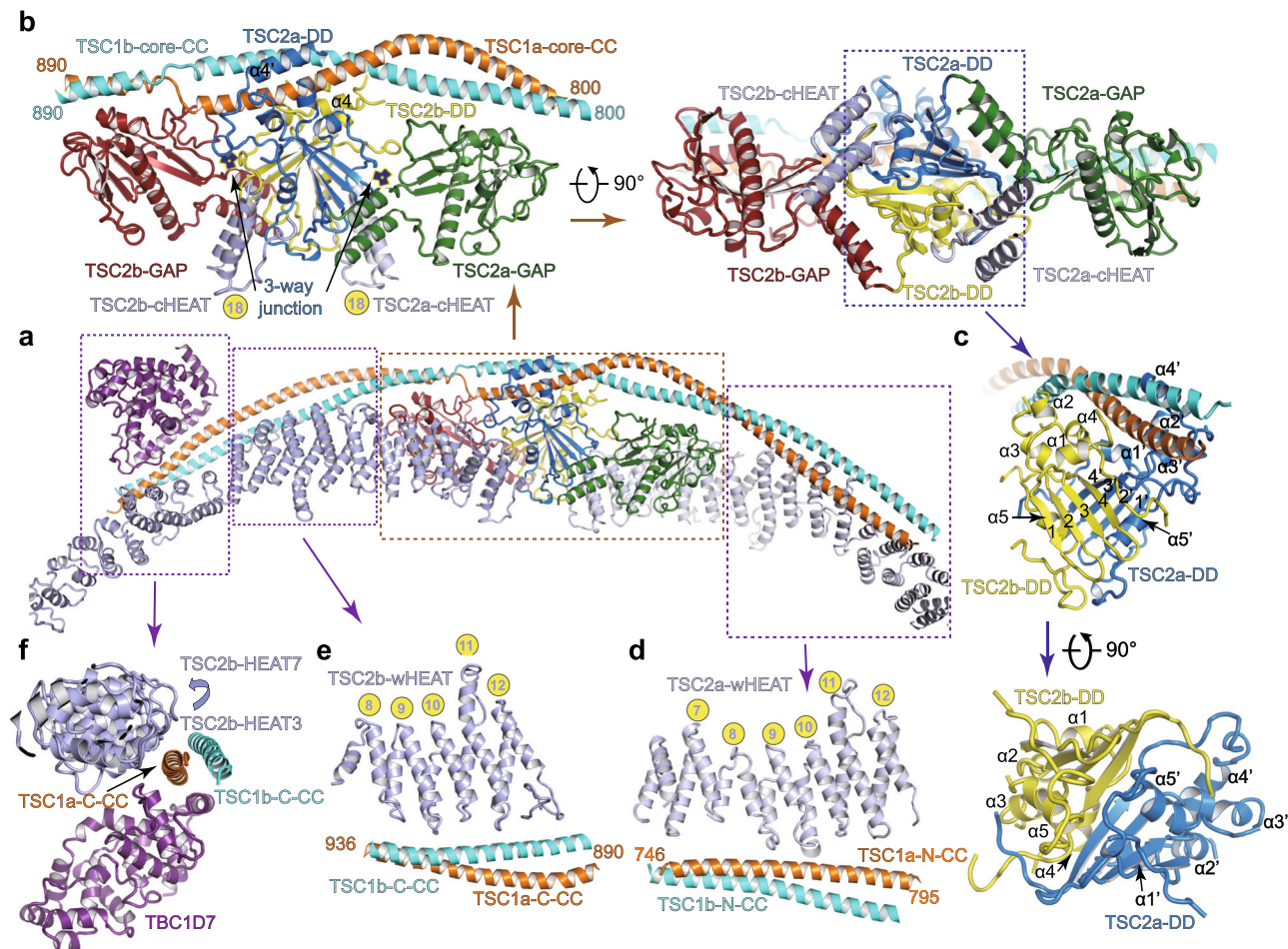


Fig. 2 Intermolecular interfaces of TSC complex. **a** Overall structure of TSC complex shown in a view different from that in Fig. 1b, intermolecular contacts shown in **(b–f)** are highlighted with dashed boxes. **b** Close-up view of the intermolecular interactions in the central core module. Close-up view of the intermolecular interactions in the dimerization domain **(c)**, wing-a **(d)**, wing-b **(e)**, and TSC1 C-CC with TBC1D7 **(f)**. Critical elements are indicated. In **(c)**, $\alpha 1$ – $\alpha 5$ and $\alpha 1'$ – $\alpha 5'$ represent α helices of TSC2b and TSC2a, respectively. The numbers (1–4 and 1'–4') represent the numbered β strands.

structure (Fig. 3b, c). Structural superimposition suggests that Rheb binds TSC2 GAP in a manner similar to that in Rap1–Rap1GAP. The catalytic helix (Ga3, K¹⁶³⁸RHLGN¹⁶⁴³) of TSC2 faces toward the catalytic cavity formed by the switch I, switch II, and P-loop of the superimposed Rheb (Fig. 3i, j). The switch I is conserved among the small G proteins (Supplementary Fig. 9b). Residue N1643 of TSC2 is similarly positioned to N290 of Rap1GAP, suggesting a shared asparagine thumb of the two GAP domains. As an equivalent of residue Y32 of Rap1 and Y32 in Ras, residue Y35 of Rheb is positioned close to N1643 and may facilitate GTP hydrolysis. The TSC2 catalytic helix is positioned similar to that of Rap1GAP in Rap1–Rap1GAP¹⁹ complex structure, suggesting a similar molecular environment in stabilizing catalytic helix in the two GAP domains (Fig. 3g, i and Supplementary Fig. 10c). It has been known that Rap1GAP forms a dimer through a DD. Although the central β -sheet of the DD domains of Rap1GAP and TSC2 could be aligned well, the DD–GAP dimers adopt distinct modular organization (Supplementary Fig. 10d).

Other residues of the catalytic helix may support the catalytic helix conformation (Fig. 3i, j). Residues K1638 and R1639 (equivalent to K285 and R286 of Rap1GAP) face toward the putative Rheb and their mutations may affect substrate binding. Residue L1641 (equivalent to I288 of Rap1GAP) faces toward the core of TSC2 GAP. H1640 (equivalent to H287 of Rap1GAP) is in proximity to and binds residue R15 of Rheb, which is consistent

with the model presented in the recent report¹⁷. The conformational stability of the equivalent catalytic helix of RasGAP is essential for its activity^{6,24}, suggesting that these catalytic helix residues may also be required for GAP activity (Fig. 3e, g, i).

We performed cell-based assay to investigate the GAP activity of TSC complex by detecting the phosphorylation of S6K1 at T389, which is well accepted to represent the level of Rheb in GTP-bound form and TSC2 GAP activity^{8,29} (Fig. 3k). The co-transfection of TSC1 and TSC2 largely decreased the level of phosphorylated-S6K1, indicating a robust GAP activity in cells (Fig. 3k, lanes 1–3). Alanine substitutions of K1638 or R1639 and tuberous sclerosis-associated mutation of K1638 showed weak to moderate defect on GAP activity (Fig. 3k, lanes 4–6). K1638N mutation may hinder substrate binding due to steric hindrance. Alanine substitutions or tuberous sclerosis-associated mutations of H1640, L1641, or N1643 on TSC2, largely impaired the GAP activity (Fig. 3k, lanes 7–12), to a level comparable to that of lacking TSC complex (Fig. 3k, lane 2).

The result is consistent with structural observation and supports the notion that TSC2 uses the asparagine thumb (N1643) to accelerate GTP hydrolysis of Rheb and residues K1638, H1640, and L1641 of the catalytic helix function in supporting the conformation of the asparagine thumb. Our structural and biochemical studies show that L1641 plays an important role in TSC2 GAP activity and confirmed the significance of residues K1638, H1640, N1643, which have been

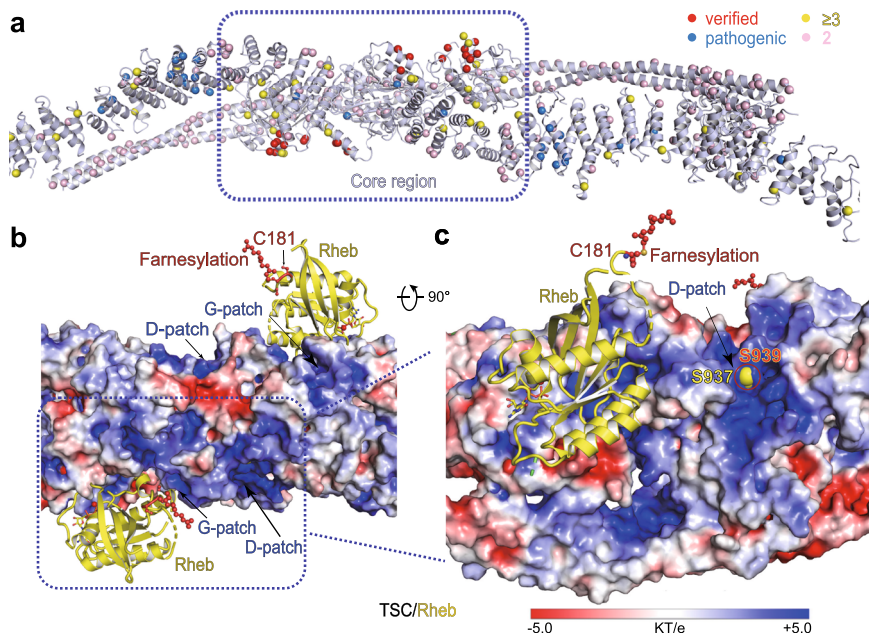


Fig. 4 TSC complex surface feature and functional implications. **a** The cartoon structure of TSC complex are shown with cancer-associated mutations highlighted with colored balls. The information of patient-derived mutations was obtained from the Catalogue of Somatic Mutations in Cancer (COSMIC)³³. Critical residues for GAP activity that were verified in our study are shown as red balls, pathogenic mutations are shown as blue balls, and the mutations identified in patients ≥ 3 and 2 times in COSMIC database are shown as yellow and pink balls, respectively. **b, c** Electrostatic potential surface of TSC complex is shown in two views. Two putative Rheb molecules (yellow) are shown in cartoon with farnesylation at C181 (red) indicated (**b**). The traced residue S937 is shown in yellow balls. The positively charged patches around dimerization domain (D-patch) and GAP domain (G-patch) are shown in a close-up view.

reported the architecture of TSC complex at a relatively lower resolution in BioRxiv, which confirmed generally similar overall fold of TSC complex in our study.

Discussion

Mutations of *TSC* genes have been frequently observed in tuberous sclerosis and cancers and missense mutations occurred throughout the protein sequences³³ (Fig. 4a and Supplementary Fig. 4). Notably, most of cancer-derived mutations and functionally important residues in *TSC2* are enriched on the central core module, supporting the pathological significance of TSC complex in these diseases. Furthermore, the identified pathogenic mutations in the wing modules are predominantly enriched on the ridges of HEAT domains of *TSC2*, consistent with their roles in mediating *TSC1*–*TSC2* interactions and TSC complex conformational stability^{21,31,34–38}.

The surface electrostatic calculations of *TSC2* structure reveals four predominant positively charged patches around the DD (D-patch) and GAP (G-patch) domains. The four patches are located on the bottom surface of the central core and close to the putative Rheb-binding pockets of the two GAP domains, suggesting a regulatory role related to its GAP function (Fig. 4b, c). It is tempting to speculate that these positively charged patches may involve charge–charge interactions and associate with negatively charged phosphorylated residues and/or lipids.

It is well documented that residue S939 of *TSC2* is phosphorylated by the AKT kinase and the phosphorylated *TSC2* is translocated from lysosomal membrane to cytosol via binding of 14-3-3 protein, and therefore inhibits GAP activity on Rheb and activates mTORC1 activity^{39,40}. Although residue S939 was invisible due to the lack of corresponding cryo-EM density, its nearest modeled residue S937 is located around the D-patch (Fig. 4c), which may recruit and stabilize the phosphorylated S939.

It is well known that inactivation of mTORC1 requires *TSC2* lysosomal localization⁴¹ and *TSC2* is recruited to lysosome membrane through nonexclusive pathways, such as binding C181 farnesylated Rheb⁴², Rag GTPases⁴³, and polycystin-1⁴⁴. Structural superimposition indicates that the farnesylated Rheb has no clash with the positive patches of *TSC2*, supporting its colocalization with TSC complex on lysosomal surface (Fig. 4b and Supplementary Fig. 8e). Lipid phosphorylation has been known to regulate membrane localization of proteins⁴⁵. TSC complex may bind phosphorylated lipid on lysosome membrane via its positive patches through charge–charge interactions, providing an alternative approach for its lysosomal localization.

Methods

Reagents. Flag-M2 affinity agarose gel was from Raygene; Mono Q and Superose 6 were from GE Healthcare; polyethylenimine (PEI) was from Polysciences (23966); HEK293A and Expi293F cells were from Invitrogen Inc.; and culture medium was from Sino Biological Inc. Antibodies against phosphorylated-S6K (Thr 389) were from Cell Signaling Technology; Flag-HRP (A8592) was from Sigma; and Horseradish peroxidase-labeled anti-mouse and anti-rabbit secondary antibodies were from AbMart.

Protein expression and purification. The ORFs of human *TSC1*, *TSC2*, and *TBC1D7* were sub-cloned into three modified pCAG vectors. The three plasmids were co-transfected to suspension Expi293F cells using PEI. After culture at 37 °C, 5% CO₂ for 3 days, cells were collected and lysed in 50 mM HEPES (pH 7.4), 300 mM NaCl, 0.2% CHAPS, 5 mM MgCl₂, 5 mM ATP, 10 mM NaF, and 3 mM DTT at 4 °C for 30 min, and the insoluble fraction was removed by centrifugation at 38,000 \times g for 30 min. Supernatants were incubated with Flag-M2 monoclonal antibody-agarose for 4 h and washed extensively. The fusion proteins (Flag-tagged *TSC1*, Myc-tagged *TSC2*, and Myc-tagged *TBC1D7*) were digested using PreScission protease overnight and the eluted proteins were further purified using ion exchange and gel filtration chromatography. The peak fractions were pooled for gradient fixation (Grafix)⁴⁶. The gradient was generated from a 10% glycerol light solution (10% (v/v) glycerol, 300 mM NaCl, 25 mM HEPES (pH 7.4), 1 mM TCEP), and a 30% glycerol heavy solution (30% (v/v) glycerol, 300 mM NaCl, 25 mM HEPES (pH 7.4), 1 mM TCEP, and 0.1% (v/v) glutaraldehyde). Centrifugation was performed at 247,605 \times g in a SW41Ti swinging bucket rotor for 18 h at 4 °C using Beckman L-100XP. Subsequently, peak fractions were collected and quenched with

100 mM Tris-HCl (pH 8.0). The cross-linked TSC complex was concentrated and dialyzed to 0.5 mg/ml for Cryo-EM grids.

Sample preparation. For negative staining EM grids preparation, 5 μ L of TSC complex sample was applied onto glow-discharged copper grids supported by a continuous thin layer of carbon film for 60 s before negatively stained by 2% (w/v) uranyl formate solution at room temperature. The grids were prepared in the Ar/O₂ mixture for 15 s using a Gatan 950 Solarus plasma cleaning system with a power of 35 W. The negatively stained grids were loaded onto a Thermo Fisher Scientific Talos L120C microscope equipped with a Ceta CCD camera and operating at 120 kV at a nominal magnification of $\times 92,000$, corresponding to a pixel size of 1.58 \AA on the specimen.

For cryo-EM grids preparation, 4 μ L of the sample at a concentration of ~ 0.5 mg/mL TSC complex was applied to freshly glow-discharged Quantifoil R1.2/1.3 holey carbon grids. After incubation of 5 s at a temperature of 4 $^{\circ}\text{C}$ and a humidity of 100%, the grids were blotted for 4–6 s in a Thermo Fisher Scientific Vitrobot Mark IV and plunge-frozen in liquid ethane at liquid nitrogen temperature. The grids were prepared in the H₂/O₂ mixture for 60 s using a Gatan 950 Solarus plasma cleaning system with a power of 5 W. The ϕ 55/20 mm blotting paper is made by TED PELLA used for plunge freezing.

Data collection. The cryo-EM grids of TSC complex were loaded onto a Thermo Fisher Scientific Titan Krios transmission electron microscope equipped with a Gatan GIF Quantum energy filter (slit width 20 eV) and operating at 300 kV for data collection. All the cryo-EM images were automatically recorded by a post-GIF Gatan K2 Summit direct electron detector in the super-resolution counting mode using Serial-EM⁴⁷ with a nominal magnification of $\times 105,000$ in the EFTEM mode, which yielded a super-resolution pixel size of 0.678 \AA on the image plane, and with a defocus ranged from 1.0 to 3.5 μm . Each micrograph stack was dose-fractionated to 32 frames with a total electron dose of ~ 50 e⁻/ \AA^2 and a total exposure time of 11.49 s. For the first data set of TSC complex sample, 3316 micrographs from a total of 3605 micrographs were selected for further processing. As for the second data set of TSC complex sample, 1381 micrographs from a total of 1546 micrographs were selected for further processing.

Image processing. For cryo-EM data, drift- and beam-induced motion correction was applied on the super-resolution movie stacks using MotionCor2⁴⁸ and binned twofold to a calibrated pixel size of 1.356 $\text{\AA}/\text{pix}$. The defocus values were estimated by Gctf⁴⁹ from summed images without dose weighting. Other procedures of cryo-EM data processing were performed within RELION v3.0^{50,51} using the dose-weighted micrographs.

For the first data sets of the TSC complex, a subset of $\sim 10,000$ particles was picked by Gautomatch (Zhang unpublished) without reference and subjected to reference-free 2D classification. Some of the resulting 2D class averages were low-pass filtered to 15 \AA and used as references for automatic particle picking of the whole data sets in RELION resulting in an initial set of 1,073,891 particles for reference-free 2D classification. In all, 510,614 particles were selected from good 2D classes for the initial 3D classification, using a 60 \AA low-pass filtered initial model from our previous cryo-EM reconstruction. After several rounds of 2D and 3D classification, 152,396 particles were 3D auto-refined and post-processed, yielding a reconstruction of TSC complex at 5.11 \AA resolution. Also, for the second data set of the TSC complex, a subset of $\sim 10,000$ particles was picked by Gautomatch (Zhang unpublished) without reference and subjected to reference-free 2D classification. Some of the resulting 2D class averages were low-pass filtered to 20 \AA and used as references for automatic particle picking of the whole data sets in RELION resulting in an initial set of 455,091 particles for reference-free 2D classification. Overall, 244,896 particles were selected from good 2D classes for the initial 3D classification, using a 60 \AA low-pass filtered initial model from our previous cryo-EM reconstruction. After several rounds of 2D and 3D classification, 71,265 particles were 3D auto-refined and post-processed, yielding a reconstruction of TSC complex at 5.22 \AA resolution. According to these reconstructions, TSC^{dataset1} and TSC^{dataset2} are the same sample. Thus, two data sets were merged to improve the map quality. After several rounds of 2D and 3D classification, 131,022 particles were 3D auto-refined and post-processed, yielding a reconstruction at 4.4 \AA resolution. We used a local mask 3D refinement for the wing-a, core, and wing-b region, 131,022 particles were local refined and post-processed, yielding a 4.1 \AA reconstruction of TSC complex wing-a region, a 3.6 \AA reconstruction of TSC complex core region, and a 3.9 \AA reconstruction of TSC complex wing-b region, respectively.

All reported resolutions are based on the gold-standard Fourier shell correlation (FSC) = 0.143 criterion. The GSFSC curves were corrected for the effects of a soft mask with high-resolution noise substitution. All cryo-EM maps were sharpened by applying a negative B-factor estimated during post-processing in RELION. All the visualization and evaluation of the 3D volume map were performed within UCSF Chimera or UCSF ChimeraX⁵², and the local resolution variations were calculated using RELION⁵⁰.

Model building and structure refinement. The cryo-EM maps of the TSC complex wing-a region complex at 4.1 \AA resolution, the TSC complex core region

complex at 3.6 \AA resolution, and the TSC complex wing-b region complex at 3.9 \AA resolution were used for model fitting. The structure of TSC1-TBCID7 (PDB: 5EJC) was used as initial structural template, which was docked into the cryo-EM maps by rigid-body fitting using UCSF Chimera⁵². The structural models were further manually built de novo in COOT⁵³ and refined in real space using Phenix⁵⁴ with secondary structure and geometry restraints using the cryo-EM map. Overfitting of the model was monitored by refining the model in one of the two half maps from the gold-standard refinement approach and testing the refined model against the other map⁵⁵. Statistics of the map reconstruction and model refinement can be found in Table 1. The final models were evaluated using MolProbity⁵⁶. Map and model representations in the figures and movies were prepared by PyMOL (<http://www.pymol.org>), UCSF Chimera, or UCSF ChimeraX⁵⁷.

In vitro GAP assay. GTPase-activating activity was determined with a calorimetric assay⁵⁸ measuring the formation of inorganic phosphate. The purified TSC complex or TSC2 GAP domain was incubated with Rheb (3 μM) in a buffer containing 25 mM Hepes (pH 7.4), 200 mM NaCl, 1 mM GTP in 50 μL reaction mixtures and incubated at 37 $^{\circ}$ for 3 h. Reactions were terminated by the addition of 100 μL of malachite green/acid molybdate solution. After 20 min of color development, OD620 was determined.

In vivo GAP assay. The HEK293A cells were transfected with Flag-S6K1, Flag-Rheb, Flag-TSC1, Myc-TBCID7, Flag-TSC2 WT, and mutants using PEI. After 48 h, the cells were collected and lysed for 30 min. The supernatant was collected by centrifuge and boiled with SDS loading buffer. The sample was conducted for western blotting. The primary antibody was incubated overnight and washed three times with TBST, and incubated with secondary antibody for 1 h. After extensive rinsing with TBST for three times, ECL was detected.

Reporting summary. Further information on research design is available in the Nature Research Reporting Summary linked to this article.

Data availability

The electron density map and corresponding atomic coordinates have been deposited in the Protein Data Bank (<http://www.rcsb.org/pdb>) under accession code: 7DL2 and in EMBD under accession codes: EMD-30708, EMD-30709, EMD-30710, and EMD-30711. Source data are provided with this paper.

Received: 19 June 2020; Accepted: 4 December 2020;

Published online: 12 January 2021

References

- Nojima, H. et al. The mammalian target of rapamycin (mTOR) partner, raptor, binds the mTOR substrates p70 S6 kinase and 4E-BP1 through their TOR signaling (TOS) motif. *J. Biol. Chem.* **278**, 15461–15464 (2003).
- Saxton, R. A. & Sabatini, D. M. mTOR signaling in growth, metabolism, and disease. *Cell* **168**, 960–976 (2017).
- Gai, Z. et al. Structure of the TBCID7-TSC1 complex reveals that TBCID7 stabilizes dimerization of the TSC1 C-terminal coiled coil region. *J. Mol. Cell Biol.* **8**, 411–425 (2016).
- Dibble, C. C. et al. TBCID7 is a third subunit of the TSC1-TSC2 complex upstream of mTORC1. *Mol. Cell* **47**, 535–546 (2012).
- van Slegtenhorst, M. et al. Interaction between hamartin and tuberlin, the TSC1 and TSC2 gene products. *Hum. Mol. Genet.* **7**, 1053–1057 (1998).
- Brownbridge, G. G., Lowe, P. N., Moore, K. J., Skinner, R. H. & Webb, M. R. Interaction of GTPase activating proteins (GAPs) with p21ras measured by a novel fluorescence anisotropy method. Essential role of Arg-903 of GAP in activation of GTP hydrolysis on p21ras. *J. Biol. Chem.* **268**, 10914–10919 (1993).
- Garami, A. et al. Insulin activation of Rheb, a mediator of mTOR/S6K/4E-BP signaling, is inhibited by TSC1 and 2. *Mol. Cell* **11**, 1457–1466 (2003).
- Inoki, K., Li, Y., Xu, T. & Guan, K. L. Rheb GTPase is a direct target of TSC2 GAP activity and regulates mTOR signaling. *Genes Dev.* **17**, 1829–1834 (2003).
- Tee, A. R., Manning, B. D., Roux, P. P., Cantley, L. C. & Blenis, J. Tuberous sclerosis complex gene products, Tuberlin and Hamartin, control mTOR signaling by acting as a GTPase-activating protein complex toward Rheb. *Curr. Biol.* **13**, 1259–1268 (2003).
- Zhang, Y. et al. Rheb is a direct target of the tuberous sclerosis tumour suppressor proteins. *Nat. Cell Biol.* **5**, 578–581 (2003).
- Castro, A. F., Rebhun, J. F., Clark, G. J. & Quilliam, L. A. Rheb binds tuberous sclerosis complex 2 (TSC2) and promotes S6 kinase activation in a rapamycin- and farnesylation-dependent manner. *J. Biol. Chem.* **278**, 32493–32496 (2003).

12. Inoki, K., Corradetti, M. N. & Guan, K. L. Dysregulation of the TSC-mTOR pathway in human disease. *Nat. Genet.* **37**, 19–24 (2005).
13. Henske, E. P., Jozwiak, S., Kingswood, J. C., Sampson, J. R. & Thiele, E. A. Tuberous sclerosis complex. *Nat. Rev. Dis. Primers* **2**, 16035 (2016).
14. Qin, J. et al. Structural basis of the interaction between tuberous sclerosis complex 1 (TSC1) and Tre2-Bub2-Cdc16 domain family member 7 (TBC1D7). *J. Biol. Chem.* **291**, 8591–8601 (2016).
15. Sun, W. et al. Crystal structure of the yeast TSC1 core domain and implications for tuberous sclerosis pathological mutations. *Nat. Commun.* **4**, 2135 (2013).
16. Zech, R., Kiontke, S., Mueller, U., Oeckinghaus, A. & Kummel, D. Structure of the tuberous sclerosis complex 2 (TSC2) N terminus provides insight into complex assembly and tuberous sclerosis pathogenesis. *J. Biol. Chem.* **291**, 20008–20020 (2016).
17. Hansmann, P. et al. Structure of the TSC2 GAP domain: mechanistic insight into catalysis and pathogenic mutations. *Structure* <https://doi.org/10.1016/j.str.2020.05.008> (2020).
18. Yu, Y. et al. Structural basis for the unique biological function of small GTPase RHEB. *J. Biol. Chem.* **280**, 17093–17100 (2005).
19. Scrima, A., Thomas, C., Deaconescu, D. & Wittinghofer, A. The Rap-RapGAP complex: GTP hydrolysis without catalytic glutamine and arginine residues. *EMBO J.* **27**, 1145–1153 (2008).
20. Gao, X. & Pan, D. TSC1 and TSC2 tumor suppressors antagonize insulin signaling in cell growth. *Genes Dev.* **15**, 1383–1392 (2001).
21. Li, Y., Inoki, K. & Guan, K. L. Biochemical and functional characterizations of small GTPase Rheb and TSC2 GAP activity. *Mol. Cell. Biol.* **24**, 7965–7975 (2004).
22. Santiago Lima, A. J. et al. Identification of regions critical for the integrity of the TSC1-TSC2-TBC1D7 complex. *PLoS ONE* **9**, e93940 (2014).
23. Hoogeveen-Westerveld, M. et al. The TSC1-TSC2 complex consists of multiple TSC1 and TSC2 subunits. *BMC Biochem.* **13**, 18 (2012).
24. Scheffzek, K. et al. The Ras-RasGAP complex: structural basis for GTPase activation and its loss in oncogenic Ras mutants. *Science* **277**, 333–338 (1997).
25. Scheffzek, K. & Ahmadian, M. R. GTPase activating proteins: structural and functional insights 18 years after discovery. *Cell Mol. Life Sci.* **62**, 3014–3038 (2005).
26. Mishra, A. K. & Lambright, D. G. Invited review: small GTPases and their GAPs. *Biopolymers* **105**, 431–448 (2016).
27. Mittal, R., Ahmadian, M. R., Goody, R. S. & Wittinghofer, A. Formation of a transition-state analog of the Ras GTPase reaction by Ras-GDP, tetrafluoroaluminate, and GTPase-activating proteins. *Science* **273**, 115–117 (1996).
28. Daumke, O., Weyand, M., Chakrabarti, P. P., Vetter, I. R. & Wittinghofer, A. The GTPase-activating protein Rap1GAP uses a catalytic asparagine. *Nature* **429**, 197–201 (2004).
29. Li, Y., Inoki, K., Vikis, H. & Guan, K. L. Measurements of TSC2 GAP activity toward Rheb. *Methods Enzymol.* **407**, 46–54 (2006).
30. Marshall, C. B. et al. Characterization of the intrinsic and TSC2-GAP-regulated GTPase activity of Rheb by real-time NMR. *Sci. Signal.* **2**, ra3 (2009).
31. Hoogeveen-Westerveld, M. et al. Functional assessment of variants in the TSC1 and TSC2 genes identified in individuals with tuberous sclerosis complex. *Hum. Mutat.* **32**, 424–435 (2011).
32. Ramlal, K. et al. Architecture of the tuberous sclerosis protein complex. *bioRxiv* <https://doi.org/10.1101/2020.09.29.319707> (2020).
33. Tate, J. G. et al. COSMIC: the catalogue of somatic mutations in cancer. *Nucleic Acids Res.* **47**, D941–D947 (2019).
34. Inoki, K., Li, Y., Zhu, T., Wu, J. & Guan, K. L. TSC2 is phosphorylated and inhibited by Akt and suppresses mTOR signalling. *Nat. Cell Biol.* **4**, 648–657 (2002).
35. Hodges, A. K. et al. Pathological mutations in TSC1 and TSC2 disrupt the interaction between hamartin and tuberin. *Hum. Mol. Genet.* **10**, 2899–2905 (2001).
36. Dufner Almeida, L. G. et al. Comparison of the functional and structural characteristics of rare TSC2 variants with clinical and genetic findings. *Hum. Mutat.* **41**, 759–773 (2020).
37. Nellist, M. et al. Distinct effects of single amino-acid changes to tuberin on the function of the tuberin-hamartin complex. *Eur. J. Hum. Genet.* **13**, 59–68 (2005).
38. Hoogeveen-Westerveld, M. et al. Functional assessment of TSC2 variants identified in individuals with tuberous sclerosis complex. *Hum. Mutat.* **34**, 167–175 (2013).
39. Manning, B. D., Tee, A. R., Logsdon, M. N., Blenis, J. & Cantley, L. C. Identification of the tuberous sclerosis complex-2 tumor suppressor gene product tuberin as a target of the phosphoinositide 3-Kinase/Akt pathway. *Mol. Cell* **10**, 151–162 (2002).
40. Cai, S. L. et al. Activity of TSC2 is inhibited by AKT-mediated phosphorylation and membrane partitioning. *J. Cell Biol.* **173**, 279–289 (2006).
41. Demetriades, C., Plescher, M. & Teleman, A. A. Lysosomal recruitment of TSC2 is a universal response to cellular stress. *Nat. Commun.* **7**, 10662 (2016).
42. Menon, S. et al. Spatial control of the TSC complex integrates insulin and nutrient regulation of mTORC1 at the lysosome. *Cell* **156**, 771–785 (2014).
43. Demetriades, C., Doumpas, N. & Teleman, A. A. Regulation of TORC1 in response to amino acid starvation via lysosomal recruitment of TSC2. *Cell* **156**, 786–799 (2014).
44. Dere, R., Wilson, P. D., Sandford, R. N. & Walker, C. L. Carboxy terminal tail of polycystin-1 regulates localization of TSC2 to repress mTOR. *PLoS ONE* **5**, e9239 (2010).
45. McLaughlin, S. & Murray, D. Plasma membrane phosphoinositide organization by protein electrostatics. *Nature* **438**, 605–611 (2005).
46. Stark, H. GraFix: stabilization of fragile macromolecular complexes for single particle cryo-EM. *Methods Enzymol.* **481**, 109–126 (2010).
47. Mastrorade, D. N. Automated electron microscope tomography using robust prediction of specimen movements. *J. Struct. Biol.* **152**, 36–51 (2005).
48. Zheng, S. Q. et al. MotionCor2: anisotropic correction of beam-induced motion for improved cryo-electron microscopy. *Nat. Methods* **14**, 331–332 (2017).
49. Zhang, K., Gctf & Real-time, C. T. F. determination and correction. *J. Struct. Biol.* **193**, 1–12 (2016).
50. Kimanius, D., Forsberg, B. O., Scheres, S. H. W. & Lindahl, E. Accelerated cryo-EM structure determination with parallelisation using GPUs in RELION-2. *Elife* **5**, 18722 (2016).
51. Scheres, S. H. W. RELION: implementation of a Bayesian approach to cryo-EM structure determination. *J. Struct. Biol.* **180**, 519–530 (2012).
52. Pettersen, E. F. et al. UCSF chimera—a visualization system for exploratory research and analysis. *J. Comput. Chem.* **25**, 1605–1612 (2004).
53. Emsley, P. & Cowtan, K. Coot: model-building tools for molecular graphics. *Acta Crystallogr. D* **60**, 2126–2132 (2004).
54. Adams, P. D. et al. PHENIX: building new software for automated crystallographic structure determination. *Acta Crystallogr. D* **58**, 1948–1954 (2002).
55. Amunts, A. et al. Structure of the yeast mitochondrial large ribosomal subunit. *Science* **343**, 1485–1489 (2014).
56. Chen, V. B. et al. MolProbity: all-atom structure validation for macromolecular crystallography. *Acta Crystallogr. D* **66**, 12–21 (2010).
57. Goddard, T. D. et al. UCSF ChimeraX: meeting modern challenges in visualization and analysis. *Protein Sci.* **27**, 14–25 (2018).
58. Cairns, B. R., Kim, Y. J., Sayre, M. H., Laurent, B. C. & Kornberg, R. D. A multisubunit complex containing the SWI1/ADR6, SWI2/SNF2, SWI3, SNF5, and SNF6 gene products isolated from yeast. *Proc. Natl Acad. Sci. USA* **91**, 1950–1954 (1994).

Acknowledgements

We thank Center of Cryo-Electron Microscopy, Fudan University, Center of Cryo-Electron Microscopy, Peking University, Center for Biological Imaging of Institute of Biophysics (IBP) of Chinese Academy of Sciences, and National Center for Protein Science Shanghai (NCPSS) for the support on cryo-EM data collection and data analyses. This work was supported by grants from the National key R&D program of China (2016YFA0500700), the National Natural Science Foundation of China (31770781, 31830107, 31821002, 32030055), the Shanghai Municipal Science and Technology Major Project (2017SHZDZX01), Shanghai Municipal Science and Technology Commission (19JC1411500), the Science and Technology Major Project of Inner Mongolia Autonomous Region of China to the State Key Laboratory of Reproductive Regulation and Breeding of Grassland Livestock, the National Ten-Thousand Talent Program, the National Program for support of Top-Notch Young Professionals, and the Strategic Priority Research Program of the Chinese Academy of Sciences (Grant No. XDB08000000).

Author contributions

H.Y. prepared the samples for structural and biochemical analyses with help from X.C., J.L., H.-X.Y., D.Y., and K.-L.G.; Z.Y. performed EM analyses and model building with the help from N.L., J.C., and N.G.; Y.X. wrote the paper with the help from H.Y. and K.-L.G.; Y.X. supervised the project.

Competing interests

The authors declare no competing interests.

Additional information

Supplementary information is available for this paper at <https://doi.org/10.1038/s41467-020-20522-4>.

Correspondence and requests for materials should be addressed to H.Y. or Y.X.

Peer review information *Nature Communications* thanks the anonymous reviewers for their contributions to the peer review of this work.

Reprints and permission information is available at <http://www.nature.com/reprints>

Publisher's note Springer Nature remains neutral with regard to jurisdictional claims in published maps and institutional affiliations.



Open Access This article is licensed under a Creative Commons Attribution 4.0 International License, which permits use, sharing, adaptation, distribution and reproduction in any medium or format, as long as you give appropriate credit to the original author(s) and the source, provide a link to the Creative Commons license, and indicate if changes were made. The images or other third party material in this article are included in the article's Creative Commons license, unless indicated otherwise in a credit line to the material. If material is not included in the article's Creative Commons license and your intended use is not permitted by statutory regulation or exceeds the permitted use, you will need to obtain permission directly from the copyright holder. To view a copy of this license, visit <http://creativecommons.org/licenses/by/4.0/>.

© The Author(s) 2021